ADVANCED ELECTRONIC MATERIALS
Open Access
www.advelectronicmat.de

Check for updates

A DC Compact Model of an Organic Electrochemical Transistor Based on a Semiconductor Physics and Thermodynamic Approach

Ermias Telahun Teka, Yeohoon Yoon, Laura Teuerle, Tommy Meier, Hans Kleemann, Ghader Darbandy, and Benjamin Iniguez*

Recent progress in printable electronics and biointerfaces has driven a growing interest in organic electronics for biosensor and neuromorphic applications, offering a valuable complement to traditional silicon technologies. Among organic electronics, organic electrochemical transistors (OECTs) have garnered significant attention for their high transconductance, biocompatibility, and dual ionic–electronic charge transport capabilities. While OECTs show strong promise, their variability due to fabrication and material inconsistencies, limited insight into charge transport, and absence of standard models hinder their integration. A robust, physics-based compact model can bridge these gaps and facilitate broader adoption of this device technology. This work presents a physics-based DC compact model for OECTs, integrating electrochemical interactions using the Nernst equation in the above threshold regime with drain bias-dependent diffusive charge transport in the subthreshold regime, unified by a hyperbolic tangent transition. It integrates the threshold voltage roll-off effect and the drain voltage-dependence of the hole mobility using the Poole–Frenkel mobility model. The model is validated against experimental data from four distinct geometries of p-type poly(3,4-ethylenedioxythiophene):polystyrene sulfonate (PEDOT: PSS) OECTs, which show excellent agreement with the measurements. The model reliably captures DC characteristics, making it suitable for incorporation into circuit simulation tools to support broader application development.

1. Introduction

Organic electrochemical transistors (OECTs) are organic transistors that have a wide range of applications in biological and neuromorphic systems. They have gained significant attention in biosensing,[1] owing to their ability to operate in aqueous environments and integrate with microfluidic systems. Their versatility has led to applications in electrophysiological sensors,[2] bioelectronic implants,[3] wearable electronic sensors[4] and lab-on-chip devices.[5] Moreover, interest in OECTs applications in advanced fields such as neuromorphic computing,[6] logic circuits,[7] smart textiles,[8] and electrochromic displays[9] has increased. This broad applicability of OECTs derives from their reversibility, low driving voltage, low power consumption, high transconductance, biocompatibility, and ability to transduce ions into electronic signals with high gain and a high signal-to-noise ratio.[10–14]

OECTs differ from organic field effect transistors (OFETs) by their use of an Organic Mixed Ionic-Electronic Conductor (OMIEC)[15] channel for ionic–electronic charge conduction. Additionally, the presence of an electrolyte between the gate and the channel enables electrochemical doping, a mechanism that sets OECTs apart from the field-effect operation of OFETs. OECTs are three-terminal devices in which a gate voltage modulates the current through the OMIEC channel via ionic exchange across an electrolyte, as illustrated in **Figure 1a**. This electrochemical interaction enables simultaneous regulation of electronic and ionic charge carriers through ionic injection from the electrolyte into

E. T. Teka, B. Iniguez
Department of Electrical and Automatic Electronic Engineering
Universitat Rovira i Virgili
Tarragona 43007, Spain
E-mail: ermiastelahun.teka@urv.cat

The ORCID identification number(s) for the author(s) of this article can be found under https://doi.org/10.1002/aelm.202500374

© 2025 The Author(s). Advanced Electronic Materials published by Wiley-VCH GmbH. This is an open access article under the terms of the Creative Commons Attribution License, which permits use, distribution and reproduction in any medium, provided the original work is properly cited.

DOI: 10.1002/aelm.202500374

Y. Yoon, L. Teuerle, T. Meier, H. Kleemann
Dresden Integrated Center for Applied Physics and Photonic Materials
Technische Universität Dresden
01062 Dresden, Germany

H. Kleemann
Micro- and Nanoelectronic Systems (MNES)
Institute of Micro- and Nanoelectronics
Technische Universität Ilmenau
98693 Ilmenau, Germany

G. Darbandy
Center of Competence for Nanotechnology and Photonics
Technische Hochschule Mittelhessen University of Applied Sciences
35390 Giessen, Germany

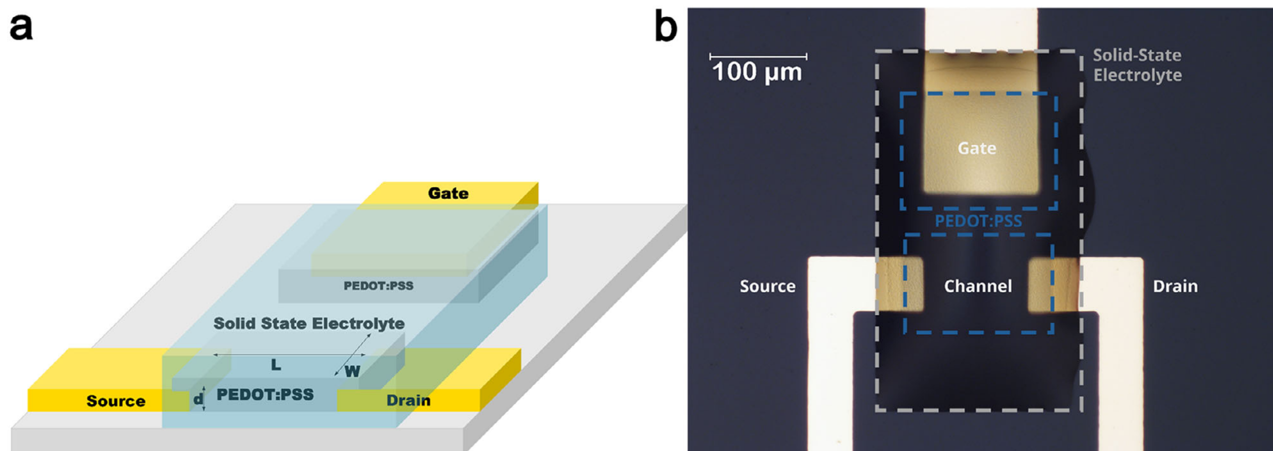

Figure 1. a) 3D schematic of the structure of an OECT. b) Image of the fabricated OECT with solid-state electrolyte and a PEDOT: PSS-based channel of length 150 µm, width 100 µm, and a gate area of 160 µm x 120 µm.

the OMIEC channel, triggering a doping–dedoping process that governs channel conductivity.[16,17]

To enable the use of OECTs in a wide range of proposed applications, a robust compact model must be developed to support circuit simulations and facilitate mass production. Although several models for DC characteristics have emerged in recent years, achieving precise validation with experimental measurements has posed significant challenges. One of the most well-known models of an organic electrochemical transistor (OECT) by Bernards et al.[18] considers only electrostatic processes and does not capture the Faradaic current that arises due to the electrochemical redox reaction. Similarly, Friedlein et al.[19] used a modified version of the Bernards model with similar shortcomings. Other works by Cucchi et al.[20] and Feitosa et al.[12] have applied thermodynamic analysis, approaching modeling from a purely electrochemical perspective and neglecting the semiconductor physics properties of OECTs, especially in the subthreshold regime. A recent work by Darbandy et al.[21] used a mixed methodology, implementing the electrochemical approach for the above threshold and the semiconductor approach for the subthreshold regimes. However, their work has important limitations, such as their incomplete implementation of the threshold voltage roll-off effect, their use of constant hole mobility, and the lack of dependence of the subthreshold current on the drain voltage, which prevents accurate fitting. Developing an accurate description of the threshold voltage, its roll-off effect, and by extension the subthreshold regime is of utmost importance for the design of energy-efficient neuromorphic circuits such as spiking neurons[22] as well as biosensing applications.[23]

In this work, we develop a physics-based DC compact model for an OECT that incorporates the drain voltage dependence of the threshold voltage with its roll-off effect as well as the bias-dependent Poole–Frenkel mobility model. The developed model was verified by experimental measurements of four different OECT geometries. This attests to the scalability of the model in different PEDOT-based OECT devices for applications in neuromorphic computing, bioelectronics, biosensors, and flexible electronics.

2. Model

2.1. Above Threshold Regime

The majority of OECT modeling strategies, such as the Bernards[18] model, rely on equivalent circuit representations to describe the coupled dynamics of electronic and ionic charge transport. However, the ionic circuit they used oversimplifies ion-to-electron transduction into an equation that assumes an ideal capacitor as the ionic reservoir.[12] This does not allow for a qualitative description of the OECTs transfer curves, their potential bistability,[3] its threshold voltage roll-off, or saturation in the transfer curve. A more accurate approach to describe OECTs ion-to-electron transduction is to use the electrochemical reaction that takes place in the channel region between the ionic charge carriers of the electrolyte and the OMIEC channel material, an intrinsically doped poly(3,4-ethylenedioxythiophene):polystyrene sulfonate (PEDOT: PSS). Numerous studies,[11,21,24,25] have outlined this electrochemical redox reaction, a dedoping-doping process, with the equation below:

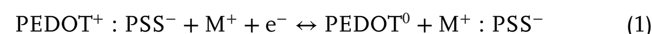

$$PEDOT^{+} : PSS^{-} + M^{+} + e^{-} \leftrightarrow PEDOT^{0} + M^{+} : PSS^{-} \quad (1)$$

When we apply a positive gate voltage, cations (M^+) from the electrolyte (e.g., Na^+, H^+, $EMIM^+$, etc.) reversibly enter the channel, neutralize PSS^- species, and hence dedope the conjugated polymer by reducing $PEDOT^+$ (oxidized state) to $PEDOT^0$ (neutral state). When we remove the gate voltage, M^+ diffuses back into the electrolyte, and PEDOT recovers to the oxidized state (doping).[26] At steady state, we can use the Nernst equation to model the quasi-equilibrium redox reaction, as has been shown in other previous works:[21,25,26,27]

$$E = E_0 + \frac{RT}{nF} ln \left(\frac{[ox]}{[red]} \right) \quad (2)$$

where E is the applied potential, E_0 is the standard potential of the redox reaction, $[ox]$ and $[red]$ are the absolute densities/concentrations of the oxidized and reduced species,

© 2025 The Author(s). Advanced Electronic Materials published by Wiley-VCH GmbH

2199160x, 0, Downloaded from https://advanced.onlinelibrary.wiley.com/doi/10.1002/aelm.202500374 by Spanish Cochrane National Provision (Ministerio de Sanidad), Wiley Online Library on [24/02/2026]. See the Terms and Conditions (https://onlinelibrary.wiley.com/terms-and-conditions) on Wiley Online Library for rules of use; OA articles are governed by the applicable Creative Commons License

respectively, R is the ideal gas constant, T is the absolute temperature, n is the number of electrons involved in the process, and F is Faraday's constant. At low concentrations, we can apply the Nernst equation to the redox reaction of Equation (2) as follows:

$$E = E_0 + \frac{RT}{nF} ln\left(\frac{\left[PEDOT^{+}:PSS^{-}+M^{+}\right]}{\left[PEDOT^{0}+M^{+}:PSS^{-}\right]}\right) \tag{3}$$

Since PEDOT is the only species reduced, and assuming that the remaining dopants and ions will balance in steady state, Equation (3) reduces to:

$$E = E_0 + \frac{RT}{nF} ln\left(\frac{\left[PEDOT^{+}\right]}{\left[PEDOT^{0}\right]}\right) \tag{4}$$

here, $[PEDOT^{+}]$ is the concentration of PEDOT in its oxidized state, and $[PEDOT^{0}]$ is the concentration of PEDOT that decreases after the PSS pairs with a cation. According to the law of conservation, the sum of the concentrations of $PEDOT^{+}$ and $PEDOT^{0}$ is the same over time and space.[20,21]

$$P^{+} + P^{0} = P_0 = constant \tag{5}$$

where P^{+}, P^{0}, and P_0 are the concentrations of $PEDOT^{+}$ (which is also the density of holes), $PEDOT^{0}$, and the total constant concentration of units of the PEDOT that take part in the redox process (which is also the density of PSS^{-}), respectively. Applying this to the Nernst equation gives:

$$E = E_0 + \frac{RT}{nF} ln\left(\frac{P^{+}}{P_0 - P^{+}}\right) \tag{6}$$

$$P^{+} = \frac{P_0}{1+e^{\frac{E-E_0}{b}}} \tag{7}$$

here, $b = RT/nF$, which is the same as the thermal voltage (kT/q) for n = 1. E and E_0 normally correspond to the potential of the working electrode of a conventional three-electrode electrochemical cell measured against a reference electrode.[27] In OECTs, we usually connect the source electrode to the ground, and the varying potential is at the gate. Therefore, we modified Equation (7) by reverting the sign of the potential and adding an additional fitting parameter (α) as follows:

$$P^{+} = \frac{P_0}{1+e^{\frac{-(V-V_{t,a})}{\alpha b}}} \tag{8}$$

The parameter α reflects the ideality factor in the model herein developed, which has a value in the range $0 < \frac{1}{\alpha} \leq 1$, representing the deviation from the ideal behavior. We then inserted Equation (8) into the drift current expression to calculate the charge in the channel based on the applied potential:

$$I = jA = Wdq\mu_h p\left(x\right) \frac{dV(x)}{dx} \tag{9}$$

where W is the channel width, d is the channel thickness, μ_h is the mobility of holes, and $p(x)$ is the concentration of the holes replaced by P^{+}. The value of the potential, V, in Equation (8) is the applied voltage at the gate and drain (i.e., V = V_G − V(x)). Hence, we calculate the drain current, $I_{D,a}$, for the above threshold regime by integrating along the channel and its potential at position x:

$$I_{D,a} \int_0^L dx = Wd\mu_h q \int_0^{V_D} \frac{P_0}{1+e^{\frac{-(V_G - V(x) - V_{t,a})}{\alpha b}}} \tag{10}$$

$$I_{D,a} = \frac{Wd}{L} \mu_h q P_0 \alpha b \left[\ln\left(e^{\frac{V_D}{\alpha b}} + e^{\frac{V_G - V_{t,a}}{\alpha b}}\right) - \ln\left(1 + e^{\frac{V_G - V_{t,a}}{\alpha b}}\right)\right] \tag{11}$$

From this equation, we can see that the above threshold model developed using the Nernst equation is dependent on both the gate and drain potentials. When we apply a high (negative) voltage at the gate, the equation simplifies to a linear relationship with the drain potential, which will be essential in extracting the hole mobility, as we discuss below. However, this equation alone does not appropriately account for the subthreshold swing, which is essential to analyze the subthreshold regime.

2.2. Subthreshold Regime

In the subthreshold regime, since the OMIEC channel is partially dedoped, the current is mostly dominated by diffusion. The electric double layer capacitance is also negligible since the gate voltage is low in the subthreshold regime.[28] Hence, we applied a semiconductor physics approach that takes into consideration the diffusive current dominant in subthreshold due to thermally activated charges. We adapted a subthreshold current equation that has previously been implemented for amorphous and organic thin film transistors.[28,29]

$$I_{D,s} = \frac{Wd}{L} \mu_h \left(\frac{SS}{\ln(10)}\right)^2 C^{*} e^{-\left(\frac{V_G - V_{t,s}}{SS/\ln(10)}\right)} \left(1 - e^{-\left(\frac{V_D}{SS/\ln(10)}\right)}\right) \tag{12}$$

where C^{*} is the volumetric capacitance of the OECT, and SS is the subthreshold slope given by $SS = \varphi \ln(10) kT/q$, and φ is a fitting parameter. We can alternatively extract the subthreshold slope from the measurement of the logarithmic transfer curve in the subthreshold regime. This subthreshold current equation accounts for the exponential carrier activation from gate bias, the diffusive transport dominated by thermal energy, and the dependence of the current on drain bias, especially for small drain voltages.

The two equations, Equations (11) and (12), only describe the corresponding above threshold and subthreshold regimes. A traditional method used for Si-based TFTs is to take $[(1/I_{D,a}) + (1/I_{D,s})]^{-1}$ as the combined equation, however this lacks the general applicability to organic transistors, particularly when the sub-to-above transition is spread over a wide voltage range.[30] We applied a hyperbolic tangent transition function as a suitable method for OECTs with a tunability of the position and the degree of transition. Finally, we constructed the unified compact model, which is valid and continuous from the subthreshold to above threshold regimes, by using the hyperbolic function given below:

$$I_D = I_{D,a} \frac{1}{2} \left\{1 - tanh\left[B\left(V_G - \left(V_t + V_{t,tr}\right)\right)\right]\right\}$$
$$+ I_{D,s} \frac{1}{2} \left\{1 + tanh\left[B\left(V_G - \left(V_t + V_{t,tr}\right)\right)\right]\right\} + I_0 \tag{13}$$

© 2025 The Author(s). Advanced Electronic Materials published by Wiley-VCH GmbH

2199160x, 0, Downloaded from https://advanced.onlinelibrary.wiley.com/doi/10.1002/aelm.202500374 by Spanish Cochrane National Provision (Ministerio de Sanidad), Wiley Online Library on [24/02/2026]. See the Terms and Conditions (https://onlinelibrary.wiley.com/terms-and-conditions) on Wiley Online Library for rules of use; OA articles are governed by the applicable Creative Commons License

We introduced the transition voltage $V_{t,tr}$ and the transition steepness parameter B as fitting parameters for accurately modeling the above-to-subthreshold transition. The sum of V_t and $V_{t,tr}$ fixes the center of the transition in the two hyperbolic tangent functions. The other term B dictates the degree of steepness or smoothness around the transition voltage. I_0 is the voltage independent off-state current. The first term in Equation (13), $I_{D,a}$, is the current from the above threshold regime of Equation (11), and the second term, $I_{D,s}$, is the current from the subthreshold regime of Equation (12). This shows that the compact model comprises an ordinary conductor switched by ions in the above threshold regime and a semiconductor switched by an electric field in the subthreshold regime.

2.3. Effective Gate Voltage

In OECTs, capacitive effects at the gate and channel–electrolyte interfaces might lead to a mismatch between the gate potential and the electrolyte potential, which affects channel conductivity modulation.[19] The electrolyte potential, i.e., the effective gate (channel) voltage, is determined by the capacitances associated with the formation of a double layer at the gate and the channel.[31] We calculate this effective gate voltage by using the capacitive divider as follows:

$$V_{G,\ eff} = \frac{V_G}{1+\sigma} \tag{14}$$

where σ is the ratio of capacitances ($\sigma = C_{CH}/C_G$ and C_{CH} and C_G are the channel and gate capacitance, respectively), which are determined from channel and gate volumes. However, since the thickness of the PEDOT: PSS on the gate and on the channel remains the same, the ratio corresponds to $\sigma = (W * L) / (W_G * L_G)$, where W and L are the channel width and length, respectively, and W_G and L_G are the gate width and length of the PEDOT: PSS layer, respectively. We used this $V_{G,\ eff}$ for all the gate voltage values in our compact model.

2.4. Threshold Voltage Roll-Off

In OECTs, the threshold voltage is primarily determined by the channel material's energy levels and the film's ability to allow ion penetration, which typically aligns with the electrochemical onset potential.[17] The threshold voltage depends on the type of gate electrode,[32] gate capacitance,[33] the type and concentration of the ion in the electrolyte,[34] channel material,[35] light exposure,[36] or geometry among other factors. Some side-gate OECTs, such as the one we are modeling, show threshold voltage roll-off behavior with increasing drain bias and a loss of saturation in the output curve.[37] Prüfer et al.[38] observed and successfully modeled the threshold voltage shift in short-channel (channel length in the submicron range) OTFTs due to drain induced barrier lowering (DIBL). However, we have observed this phenomenon in OECTs with channel lengths of even 150 µm.

In OECTs, the lateral drain-source field induces ionic capacitive coupling between the electrodes that leads to threshold voltage roll-off, i.e., an increase in the threshold voltage with increasing drain voltage, in the transfer curve, and the loss of current saturation in the output curve with increasing drain-source voltage, a phenomenon known as electrochemical electrode coupling (EEC). Weissbach et al.[39] have shown that decreasing the drain / OMIEC overlap and using a nonpolarizable gate electrode lowers the EEC.

From measurements, we observed that the threshold voltage roll-off can be modeled using an empirical second-degree polynomial equation, as given below.

$$V_t = \eta V_D^2 + \gamma V_D + V_{t0} \tag{15}$$

where η and γ are roll-off parameters extracted from the measurement data shown in **Figure 2** and V_{t0} is the zero drain-bias threshold voltage of the above threshold regime extracted from measurement data. The threshold voltage obtained from this equation is the one that we use in Equations (11) and (13).

To extract the threshold voltage for the above threshold regime, we used the peak transconductance method[40] as shown in Figure S1a (Supporting Information). For the subthreshold regime, we extracted a second threshold voltage via the second derivative method[41] as shown in Figure S1b (Supporting Information). Since we applied two different equations for the above threshold and subthreshold regimes, we needed two different methods to extract the respective threshold voltages.

In addition, we determined the gate turn-off voltage to be the voltage at which any further increase in the gate voltage only amounted to a leakage current and no further decrease in the corresponding drain current. We found this point by using the minimum of the derivative (slope) of the logarithmic transfer curve and used it to identify and quantify the threshold voltage roll-off relationship, i.e., η and γ. As we increased the drain voltage, the gate turn-off voltage also increased, as shown in Figure 2, but in a nonlinear manner, which we extracted into Equation (15). We also used this gate turn-off voltage to extract the off-state current.

2.5. Hole Mobility

We directly extracted the hole mobility from the measurement of the linear transfer characteristic curve. In Equation (11), as V_G increases to the maximum value ($\lim_{V_G \to -\infty} I_{D,a}$), the equation becomes linear with V_D. Hence, the hole mobility can be extracted by using the measured values of the drain voltage, drain current, and other constant device parameters.

$$\lim_{V_G \to -\infty} I_{D,a} = \frac{Wd}{L} \mu_h q P_0 V_D \tag{16}$$

This extracted hole mobility is dependent on the assumed value of P_0, the initial density of holes, on the aspect ratio, and the applied drain voltage. Hence, we cannot independently extract μ_h apart from the assumed value of P_0. However, it is very essential in determining the dependence of the hole mobility and its value in the context of the developed model. We modeled the dependence of the extracted hole mobility on different drain voltages using a Poole–Frenkel mobility model. It is a model that gives the mobility to be exponentially dependent on the applied lateral

© 2025 The Author(s). Advanced Electronic Materials published by Wiley-VCH GmbH

2199160x, 0, Downloaded from https://advanced.onlinelibrary.wiley.com/doi/10.1002/aelm.202500374 by Spanish Cochrane National Provision (Ministerio de Sanidad), Wiley Online Library on [24/02/2026]. See the Terms and Conditions (https://onlinelibrary.wiley.com/terms-and-conditions) on Wiley Online Library for rules of use; OA articles are governed by the applicable Creative Commons License

2199160x, 0, Downloaded from https://advanced.onlinelibrary.wiley.com/doi/10.1002/aelm.202500374 by Spanish Cochrane National Provision (Ministerio de Sanidad), Wiley Online Library on [24/02/2026]. See the Terms and Conditions (https://onlinelibrary.wiley.com/terms-and-conditions) on Wiley Online Library for rules of use; OA articles are governed by the applicable Creative Commons License

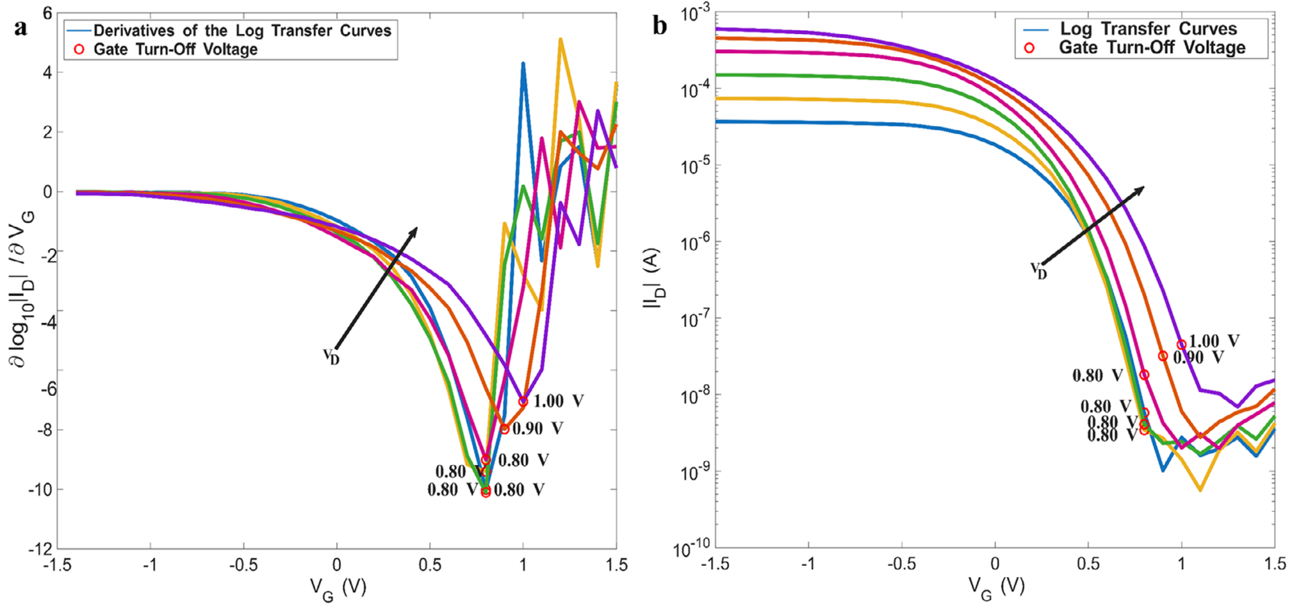

Figure 2. The gate turn-off voltage was determined by using the minimum derivative of the logarithmic transfer curve for drain voltages of −0.05, −0.1, −0.2, −0.4, and −0.6 V for an OECT with a channel length of 150 µm and a channel width of 100 µm. a) the derivative of the logarithmic transfer curve, where the minimum value gives the gate turn-off voltage. b) the corresponding logarithmic transfer curve with the gate turn-off voltage identified for increasing drain voltages.

electric field (therefore, the drain voltage),[42] as given by Equation (17) below.

$$\mu_h = \mu_0 e^{\frac{\beta \sqrt{V_d/L}}{(kT/q)}} \quad (17)$$

where μ_0 is the zero field mobility, β is the Poole–Frenkel coefficient ($\beta = \sqrt{q/\pi\epsilon\epsilon_0}$, used as a fitting parameter), L is the channel length, and kT/q is the thermal voltage. This is the value of the hole mobility implemented into Equations (11) and (12) for drain current calculations.

As shown in **Figure 3a** below, the applied mobility model was a good fit for the extracted values of the hole mobility. From the equation of the Poole–Frenkel mobility model, we determine the relationship between the mobility and the drain voltage using the extracted parameters of μ_0, the zero field mobility and β, the Poole–Frenkel coefficient.

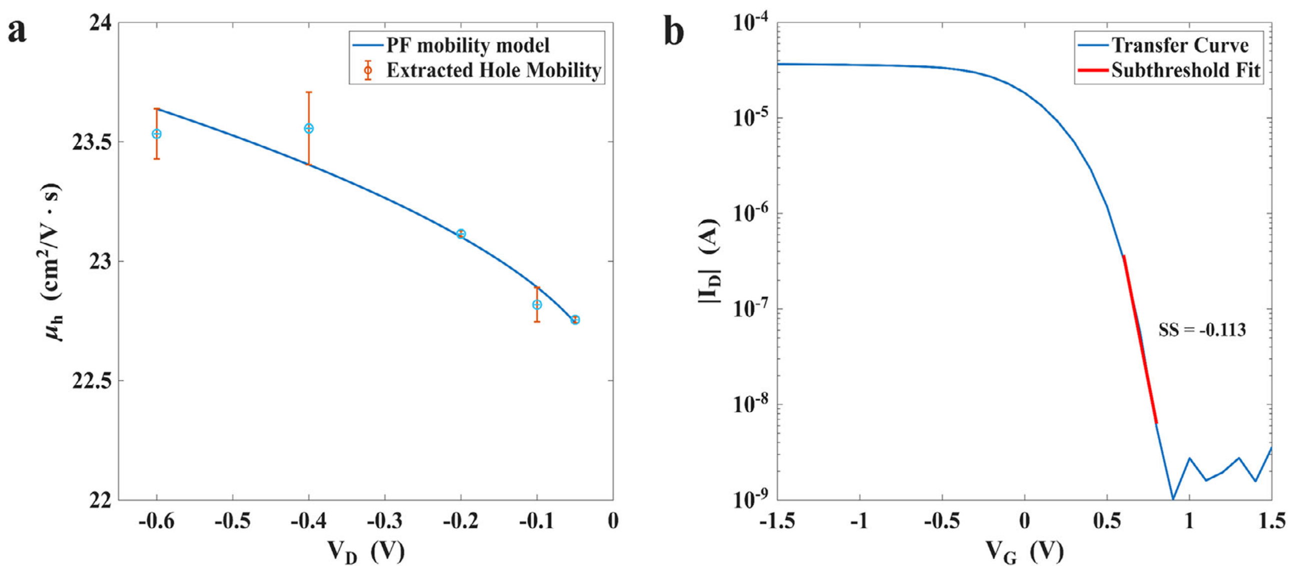

Figure 3. a) The extracted hole mobility of an OECT with a channel length of 150 µm and channel width of 100 µm in comparison with the applied Poole–Frenkel mobility model with its corresponding error bar. b) the subthreshold slope extracted using a linear fit in the subthreshold regime of the logarithmic transfer curve for an OECT with channel length of 150 µm and channel width of 100 µm for an applied drain voltage of −0.05 V.

© 2025 The Author(s). Advanced Electronic Materials published by Wiley-VCH GmbH

2199160x, 0, Downloaded from https://advanced.onlinelibrary.wiley.com/doi/10.1002/aelm.202500374 by Spanish Cochrane National Provision (Ministerio de Sanidad), Wiley Online Library on [24/02/2026]. See the Terms and Conditions (https://onlinelibrary.wiley.com/terms-and-conditions) on Wiley Online Library for rules of use; OA articles are governed by the applicable Creative Commons License

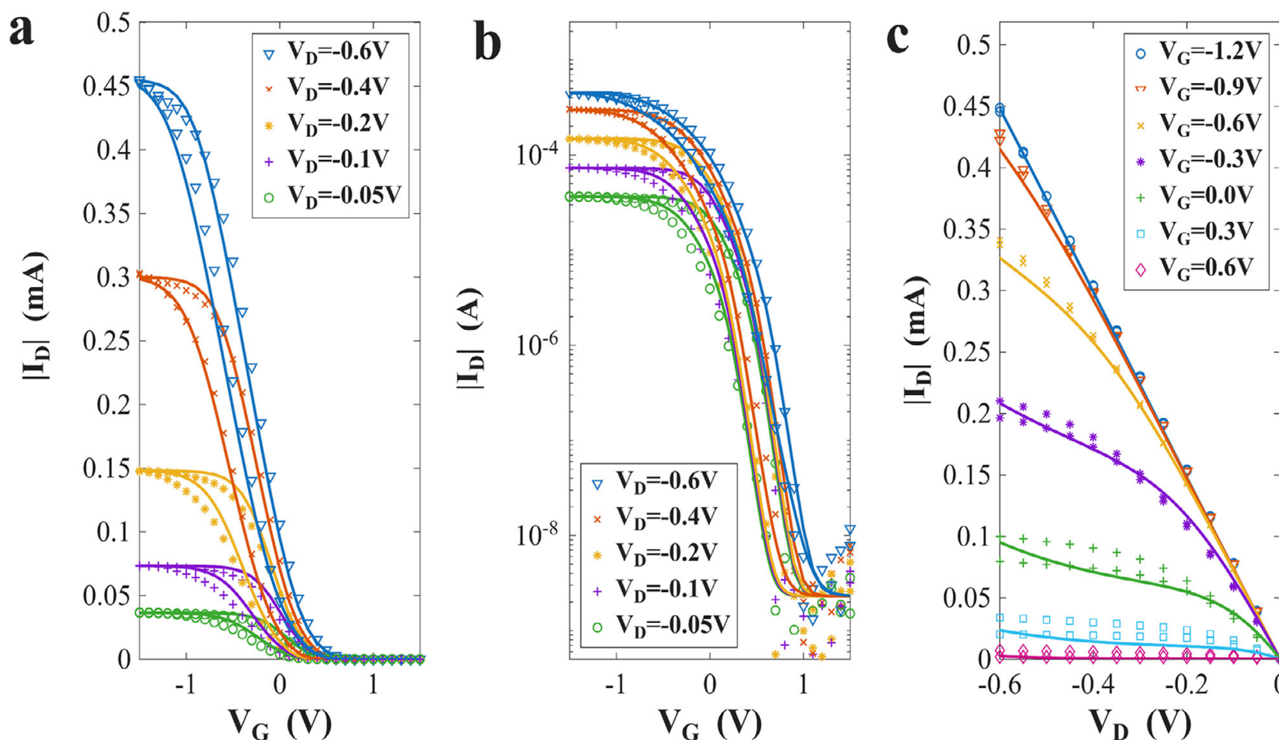

Figure 4. Comparison of measurements (symbols) and compact models (solid lines) for the forward (upper: on → off) and reverse (lower: off → on) sweeps with a channel length of 150 µm, a channel width of 100 µm, and a gate area of 160 µm x 120 µm. a) Linear transfer curves for drain voltages of −0.05, −0.1, −0.2, −0.4, and −0.6 V b) Logarithmic transfer curves with the same drain voltages as in a. c) Output curves with gate voltages of −1.2, −0.9, −0.6, −0.3, 0, 0.3, and 0.6 V.

3. Results and Discussion

We compared the results obtained from the compact model with the measurements of four different geometries of *p*-type OECTs for the linear and logarithmic DC transfer characteristics curves, as well as the output characteristics curves. We applied the key parameters we extracted, the hole mobility, the subthreshold slope (as shown in Figure 3b, extracted from the linear interpolation of the subthreshold regime of the logarithmic transfer curve), and the threshold voltage to the model. We have also incorporated into the model the effects of the threshold voltage roll-off, Poole–Frenkel field-dependent mobility model, and the effective gate voltage due to the capacitive properties of the electrolyte. Table S1 (Supporting Information) shows the different parameters that were used for the compact model. It outlines the geometrical parameters, the assumed material parameters such as the volumetric capacitance and initial hole density, the extracted model parameters, and fitting parameters. The fitting parameters and the extracted (modeled) parameters have their corresponding standard error percentages calculated based on the accuracy and sensitivity of each parameter. Although the transition voltage parameter seems to have a high global relative standard error and hence less sensitivity, it is more sensitive and accurate in the subthreshold regime and doesn't affect the overall unified model as much.

We first validated the model for the forward sweep (−1.5 → 1.5 V) of the linear and logarithmic transfer curves of an OECT with a channel length of 150 µm and a width of 100 µm. We also validated the model for the output curves, as shown in **Figure 4**. We then applied the model to the reverse sweep (1.5 → −1.5 V) of the same device by only changing the threshold voltage and transition voltage parameters, as shown in Table S1 (Supporting Information). The fit of the reverse sweep is shown in Figure 4. The model was able to show the bistability, the forward and reverse sweeps, of the PEDOT: PSS OECT by only changing the threshold and transition voltages.

We also applied the model to three other OECTs of different geometries (L = 70 µm W = 190 µm, L = 90 µm W = 100 µm, L = 70 µm W = 100 µm) with different parameter values. The parameter values and the validation of the model for these geometries are provided in the Supporting Information Section.

We observed that for the devices with the same channel widths, as the channel length increased, the dominant threshold voltage roll-off factor, γ also tended to increase. The model had an overall Root Mean Square Error (RMSE) of 5.72 µA. However, when we look at the regime specific RMSE, it is 5.97 µA for the above threshold regime and 56.33 nA for the subthreshold regime. This shows that the model is a good fit over the entire regime of the OECT transfer characteristics curve.

4. Conclusion

OECTs have gained a lot of attention in the past couple of years due to their ability to transduce ionic to electronic current. However, a modeling technique that incorporates their electro-

© 2025 The Author(s). Advanced Electronic Materials published by Wiley-VCH GmbH

chemical and semiconducting properties hasn't been properly developed. In this work, we presented and successfully validated a compact model for the DC characteristics of an OECT with experimental measurements. The model considers the redox reaction for the above threshold regime and a semiconductor physics based diffusive current for the subthreshold regime. The model was further enhanced by applying the effects of threshold voltage roll-off, effective gate voltage due to the capacitive properties of the electrolyte, and the dependence of the hole mobility with drain voltage based on the field-dependent Poole–Frenkel mobility model. A direct extraction of parameters was performed on key parameters, such as the hole mobility, subthreshold slope, and threshold voltage.

The model was able to fit the hysteresis of an OECT by simply changing the threshold and transition voltage and fitting the forward and reverse sweeps of the transfer curves. The model has been validated on a *P*-type depletion mode OECT that has a PEDOT: PSS channel and a side gate configuration with a Solid-State electrolyte. Despite the validation being limited to this architecture, it can be extended to other P-type depletion mode OECTs by simply adjusting material-specific fitting parameters.

5. Experimental Section

Device Fabrication: The compact model was developed and validated based on measurements taken of OECT devices fabricated using a previously reported hybrid OECT fabrication technique.[43] In brief, the gate, source, and drain electrodes were structured in a side-gate configuration by photolithography (SÜSS Microtec MJB4) using positive photoresist (AZ1518) and wet etching onto a glass substrate (1-inch x 1-inch) with Cr/Au (3/ 50 nm) layers. A 1% aqueous dispersion of PEDOT: PSS (Clevios PH1000) was utilized with a 5% v/v ethylene glycol solution via spin-coating at 3000 rpm for 60s to yield a thickness of 75 nm. This layer of PEDOT: PSS was then structured by photolithography for the channel region and also covered the gate electrode, to enable effective gating. For the electrolyte, five layers of an in-house developed solid-state electrolyte based on the ionic liquid 1-ethyl-3-methylimidazolium ethyl sulfate [EMIM][EtSO4] (Sigma–Aldrich) were applied through inkjet printing.[11] Figure 1b shows an image of the layout of the fabricated OECT with a channel length and a channel width defined by the dimensions of the Au electrode of 100 µm each. To ensure reliable fabrication of the device, the planar dimensions of the PEDOT: PSS layer defining the channel were 150 and 100 µm, and thus, larger than the channel length defined by the metal electrodes. The lateral size of 160 by 120 µm, the area of the PEDOT: PSS layer on the gate, was larger than the channel area, ensuring efficient gating.

Device Characterization: The *I–V* Characteristics of the OECTs were measured in a nitrogen-filled glovebox with two Keithley 236 Source Measure Units controlled via the SweepMe! software (sweep-me.net).

Supporting Information

Supporting Information is available from the Wiley Online Library or from the author.

Acknowledgements

This work was funded by the European Union under contract 101099555 (BAYFLEX) and the Ministry of Science of Spain under contracts TED2021-130307B-I00 and PRX21/00726 with the support of the predoctoral program AGAUR-FI ajuts (2023 FI-1 01022) Joan Oro of the Secretariat of Universities and Research of the Department of Research and Universities of the Generalitat de Catalunya and the European Social Funds Plus.

Conflict of Interest

The authors declare no conflict of interest.

Data Availability Statement

The data that support the findings of this study are available from the corresponding author upon reasonable request.

Keywords

DC compact model, neuromorphic devices, organic electrochemical transistor (OECT), organic mixed ionic-electronic conductor (OMIEC)

Received: June 2, 2025
Revised: August 2, 2025
Published online:

[1] J. Ajayan, P. Mohankumar, R. Mathew, L. R. Thoutam, B. K. Kaushik, D. Nirmal, *IEEE Trans. Electron Devices* **2023**, *70*, 3401.
[2] D. Khodagholy, T. Doublet, P. Quilichini, M. Gurfinkel, P. Leleux, A. Ghestem, E. Ismailova, T. Hervé, S. Sanaur, C. Bernard, G. G. Malliaras, *Nat. Commun.* **2013**, *4*, 1575.
[3] L. M. Bongartz, R. Kantelberg, T. Meier, R. Hoffmann, C. Matthus, A. Weissbach, M. Cucchi, H. Kleemann, K. Leo, *Nat. Commun.* **2024**, *15*, 6819.
[4] J. Ji, J. Xiao, F. Zhang, Z. Wang, T. Zhou, X. Niu, W. Zhang, S. Sang, X. Chai, S. Yan, *J. Nanobiotechnol.* **2025**, *23*, 120.
[5] S. Y. Yang, J. A. DeFranco, Y. A. Sylvester, T. J. Gobert, D. J. Macaya, R. M. Owens, G. G. Malliaras, *Lab Chip* **2009**, *9*, 704.
[6] L. Zhu, J. Lin, Y. Zhu, J. Wu, X. Wan, H. Sun, Z. Yu, Y. Xu, C. Tan, *Nanomaterials* **2024**, *14*, 1195.
[7] H. Sun, M. Vagin, S. Wang, X. Crispin, R. Forchheimer, M. Berggren, S. Fabiano, *Adv. Mater.* **2018**, *30*, 1704916.
[8] R. Brendgen, C. Graßmann, S. Gellner, A. Schwarz-Pfeiffer, *Micromachines (Basel)* **2022**, *13*, 1980.
[9] P. Andersson Ersman, R. Lassnig, J. Strandberg, D. Tu, V. Keshmiri, R. Forchheimer, S. Fabiano, G. Gustafsson, M. Berggren, *Nat. Commun.* **2019**, *10*, 5053.
[10] W. Huang, J. Chen, Y. Yao, D. Zheng, X. Ji, L.-W. Feng, D. Moore, N. R. Glavin, M. Xie, Y. Chen, R. M. Pankow, A. Surendran, Z. Wang, Y. Xia, L. Bai, J. Rivnay, J. Ping, X. Guo, Y. Cheng, T. J. Marks, A. Facchetti, *Nature* **2023**, *613*, 496.
[11] A. Weissbach, L. M. Bongartz, M. Cucchi, H. Tseng, K. Leo, H. Kleemann, *J. Mater. Chem. C* **2022**, *10*, 2656.
[12] B. A. de Feitosa, B. B. M. Torres, M. Luginieski, D. J. Coutinho, G. C. Faria, *Mater. Horiz.* **2024**, *11*, 6007.
[13] V. Kaphle, P. R. Paudel, D. Dahal, R. K. Radha Krishnan, B. Lüssem, *Nat. Commun.* **2020**, *11*, 2515.
[14] D. Khodagholy, J. Rivnay, M. Sessolo, M. Gurfinkel, P. Leleux, L. H. Jimison, E. Stavrinidou, T. Herve, S. Sanaur, R. M. Owens, G. G. Malliaras, *Nat. Commun.* **2013**, *4*, 2133.
[15] J. Tropp, D. Meli, J. Rivnay, *Cell Press.* **2023**, *6*, 3132.
[16] A. Marks, S. Griggs, N. Gasparini, M. Moser, *Adv. Mater. Interfaces* **2022**, *9*, 2102039.
[17] D. Ohayon, V. Druet, S. Inal, *Chem. Soc. Rev.* **2023**, *52*, 1001.
[18] D. A. Bernards, G. G. Malliaras, *Adv. Funct. Mater.* **2007**, *17*, 3538.
[19] J. T. Friedlein, R. R. McLeod, J. Rivnay, *Org. Electron.* **2018**, *63*, 398.
[20] M. Cucchi, A. Weissbach, L. M. Bongartz, R. Kantelberg, H. Tseng, H. Kleemann, K. Leo, *Nat. Commun.* **2022**, *13*, 4514.
[21] G. Darbandy, M. Koch, L. M. Bongartz, K. Leo, H. Kleemann, A. Kloes, *IEEE J. Electron Devices Soc.* **2024**, *13*, 34.

© 2025 The Author(s). Advanced Electronic Materials published by Wiley-VCH GmbH

2199160x, 0, Downloaded from https://advanced.onlinelibrary.wiley.com/doi/10.1002/aelm.202500374 by Spanish Cochrane National Provision (Ministerio de Sanidad), Wiley Online Library on [24/02/2026]. See the Terms and Conditions (https://onlinelibrary.wiley.com/terms-and-conditions) on Wiley Online Library for rules of use; OA articles are governed by the applicable Creative Commons License

[22] L. E. Calvet, O. Renard, C. Hepburn, *ECS J. Solid State Sci. Technol.* **2020**, *9*, 115004.
[23] V. Venkatraman, J. T. Friedlein, A. Giovannitti, I. P. Maria, I. McCulloch, R. R. McLeod, J. Rivnay, *Adv. Sci.* **2018**, *5*, 1800453.
[24] L. M. Bongartz, M. Cucchi, K. Leo, H. Kleemann, Proc. SPIE 12210, *Organic and Hybrid Sensors and Bioelectronics XV*, San Diego, California, USA, Oct **2022**, https://doi.org/10.1117/12.2633291.
[25] N. D. Robinson, P.-O. Svensson, D. Nilsson, M. Berggren, *J. Electrochem. Soc.* **2006**, *153*, H39.
[26] P. Lin, F. Yan, H. L. W. Chan, *ACS Appl. Mater. Interfaces* **2010**, *2*, 1637.
[27] A. Shirinskaya, G. Horowitz, J. Rivnay, G. G. Malliaras, Y. Bonnassieux, *Biosensors (Basel)* **2018**, *8*, 103.
[28] D. Tu, L. Herlogsson, L. Kergoat, X. Crispin, M. Berggren, R. Forchheimer, *IEEE Trans. Electron Devices* **2011**, *58*, 3574.
[29] M. D. Jacunski, M. S. Shur, A. A. Owusu, T. Ytterdal, M. Hack, B. Iniguez, *IEEE Trans. Electron Devices* **1999**, *46*, 1146.
[30] Chang Hyun Kim, A. Castro-Carranza, M. Estrada, A. Cerdeira, Y. Bonnassieux, G. Horowitz, B. Iniguez, *IEEE Trans. Electron Devices* **2013**, *60*, 1136.
[31] D. A. Bernards, D. J. MacAya, M. Nikolou, J. A. Defranco, S. Takamatsu, G. G. Malliaras, *J. Mater. Chem.* **2008**, *18*, 116.
[32] S. T. M. Tan, G. Lee, I. Denti, G. LeCroy, K. Rozylowicz, A. Marks, S. Griggs, I. McCulloch, A. Giovannitti, A. Salleo, *Adv. Mater.* **2022**, *34*, 2202359.
[33] H. Tseng, A. Weissbach, J. Kucinski, A. Solgi, R. Nair, L. M. Bongartz, G. Ciccone, M. Cucchi, K. Leo, H. Kleemann, *Adv. Mater. Interfaces* **2023**, *10*, 2201914.
[34] P. Romele, M. Ghittorelli, Z. M. Kovács-Vajna, F. Torricelli, *Nat. Commun.* **2019**, *10*, 3044.
[35] D. Priyadarshini, C. Li, R. Rilemark, T. Abrahamsson, M. J. Donahue, X. Strakosas, F. Ek, R. Olsson, C. Musumeci, S. Fabiano, M. Berggren, E. Olsson, D. T. Simon, J. Y. Gerasimov, *Adv. Electron. Mater.* **2024**, *36*, 2400681.
[36] Y. Wang, W. Shan, H. Li, Y. Zhong, S. Wustoni, J. Uribe, T. Chang, V. E. Musteata, T. C. H. Castillo, W. Yue, H. Ling, N. El-Atab, S. Inal, *Nat. Commun.* **2025**, *16*, 1615.
[37] A. Solgi, A. Weissbach, Y. Asl Soleimani, Y. Yoon, G. Krauss, T. Meier, H. Tseng, M. Thelakkat, K. Leo, H. Kleemann, *Adv. Electron. Mater.* **2024**, *11*, 2400656.
[38] J. Pruefer, J. Leise, G. Darbandy, A. Nikolaou, H. Klauk, J. W. Borchert, B. Iniguez, T. Gneiting, A. Kloes, *IEEE Trans. Electron Devices* **2020**, *67*, 5082.
[39] A. Weissbach, M. Cucchi, H. Tseng, K. Leo, H. Kleemann, *Adv. Funct. Mater.* **2023**, *33*, 2302205.
[40] Y. Park, S. Pandey, *IEEE Sens. J.* **2023**, *23*, 29042.
[41] A. Ortiz-Conde, F. J. García Sánchez, J. J. Liou, A. Cerdeira, M. Estrada, Y. Yue, *Microelectron. Reliab.* **2002**, *42*, 583.
[42] G. Horowitz, *Adv. Mater.* **1998**, *10*, 365.
[43] T. Meier, Y. Yoon, L. Teuerle, A. Solgi, K. Leo, H. Kleemann, *MRS Commun.* **2024**, *14*, 149.

© 2025 The Author(s). Advanced Electronic Materials published by Wiley-VCH GmbH

2199160x, 0, Downloaded from https://advanced.onlinelibrary.wiley.com/doi/10.1002/aelm.202500374 by Spanish Cochrane National Provision (Ministerio de Sanidad), Wiley Online Library on [24/02/2026]. See the Terms and Conditions (https://onlinelibrary.wiley.com/terms-and-conditions) on Wiley Online Library for rules of use; OA articles are governed by the applicable Creative Commons License